IOP Conf. Series: Materials Science and Engineering **1302** (2024) 012001 doi:10.1088/1757-899X/1302/1/012001

High-cycle fatigue strength of 22Cr-12Ni austenitic stainless steel at 77 K

M E Bratasena[1], T Kato[1], O Umezawa[2], Y Ono[3] and M Komatsu[3]

[1] Graduate School of Engineering, Yokohama National University, 79-5 Tokiwadai, Hodogaya, Yokohama, 240-8501, Japan
[2] Faculty of Engineering, Yokohama National University, 79-5 Tokiwadai, Hodogaya, Yokohama, 240-8501, Japan
[3] National Institute for Materials Science, 1-2-1 Sengen, Tsukuba, 305-0047, Japan

Email: umezawa-osamu-fv@ynu.ac.jp

Abstract. The high-cycle fatigue strength of 22Cr-12Ni austenitic stainless steel was evaluated at 77 K for three types of materials with partially recrystallized (PR), finely recrystallized (FR), and solution-treated (ST) microstructures. Subsurface crack initiation was detected at the lower stress level and/or higher cycles in the materials, such that the fatigue crack initiation sites were shifted from the specimen surface to the interior of the specimen with increasing cycles. The ST showed a significant decrease in fatigue strength over 10^6 cycles due to subsurface crack initiation. Both PR and FR showed a significant improvement in their high-cycle fatigue strength in the high-cycle regime, although the increase in fatigue strength in the low-cycle regime was approximately equal to the increase in tensile strength.

1. Introduction

Structural support materials for superconducting coils in fusion reactors, particularly the toroidal field coils, must exhibit superior strength and toughness at cryogenic temperatures. ASME standard XM-19 (22Cr-12Ni-5Mn-2Mo-0.2V-0.2Nb-0.3N, in mass%) stainless steel is strengthened by nitrogen solid solution and grain refinement with (Nb,V) precipitates. The XM-19 steel is the most promising candidate for high-strength cryogenic structural components because it has the advantages of high strength and good weldability [1]. The cryogenic tensile properties of XM-19 steel plates were dependent on their thickness [2]. The elongation and reduction of area for the extra thick plates were very low at 4 K. In particular, the mid-thickness positions showed poor ductility at both 77 K and 4 K. Therefore, the diffusion of Nb during hot rolling and solution treatment may be insufficient due to its central segregation in the cast. On the other hand, the 0.2% proof stress of the steels was related to their grain size by the Hall-Petch relationship, so grain refinement is effective for strengthening XM-19 steel at cryogenic temperature [2].

Nitrogen-strengthened austenitic steels showed a sharp decrease in high-cycle fatigue strength due to subsurface crack initiation at cryogenic temperatures [3,4]. Intergranular cracking was responsible for the subsurface crack initiation due to local stress concentration at grain boundaries [5]. A microstructural design to improve high-cycle fatigue strength has been proposed for nitrogen strengthened austenitic steels [6,7],

where grain refinement and pre-existing dislocations can promote more homogeneous deformation and reduce strain incompatibility at grain boundaries. However, few studies have been conducted on the fatigue strength and fracture of XM-19 steel at cryogenic temperatures. In this study, the high-cycle fatigue properties of fully homogenized XM-19 steel at 77 K were evaluated and the effect of grain size on fatigue strength was discussed.

2. Experimental Procedure

2.1. Materials

The chemical composition of the XM-19 test steel is shown in Table 1. The 180 kg steel ingot of ϕ210～ϕ250 × 525 mm was hot-forged into the rectangular block in a square of 150 mm and hot-rolled. The 30-mm-thick plate, solution-treated at 1373 K for 21.6 ks, was provided in a square of 30 mm and cold-groove-rolled into a rectangular bar in a square of 14.3 mm. The rectangular bars were annealed at 1173, 1273, and 1373 K for 3.6 ks and then air cooled. Their average austenite grain diameters were approximately 3.3 μm for the partially recrystallized (PR), 8.9 μm for the finely recrystallized (FR), and 42.5 μm for the solution-treated (ST). Their tensile properties such as 0.2% proof stress ($\sigma_{0.2}$), ultimate tensile strength (σ_B), total elongation (EL), and reduction of area (RA) are summarized in Table 2 [2].

Table 1. Chemical composition of the test steel (in mass%).

C	Si	Mn	P	S	Ni	Cr	Mo	V	Nb	N
0.015	0.430	5.47	0.016	0.002	13.32	21.82	1.82	0.11	0.100	0.291

Table 2. Tensile properties of the test steel at 77 K.

Materials	$\sigma_{0.2}$ (MPa)	σ_B (MPa)	EL (%)	RA (%)
PR	1368	1784	34	15
FR	1215	1689	45	36
ST	986	1592	53	31

2.2. Fatigue tests and analyses

The test specimen configuration is shown in Figure 1; unnotched hourglass-type specimens with a waist diameter of 4 mm were used. The longitudinal direction of the specimens was parallel to the rolling direction. Using a cryogenic servohydraulic fatigue testing machine, load-controlled high-cycle fatigue tests were carried out at 77 K (specimens immersed in liquid nitrogen). The sinusoidal waveform loading was uniaxial with a minimum-to-maximum stress ratio of R=0.01 and frequencies of 10 Hz. The fatigue tests were interrupted at 2 x 10^7 cycles. Fracture surfaces were analyzed by scanning electron microscopy (SEM) with energy dispersive X-ray spectroscopy (EDS).

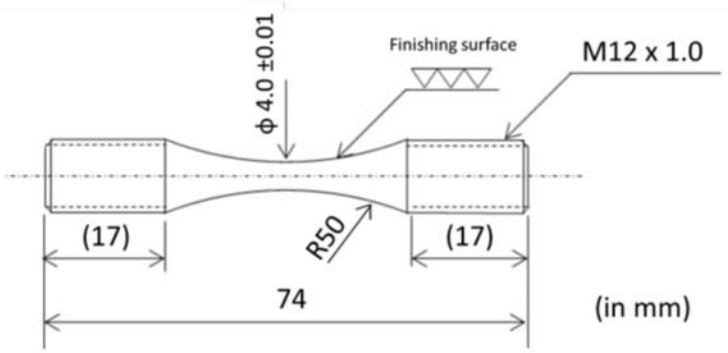

Figure 1. Configuration of fatigue test specimen.

3. Results and Discussion

3.1. Fatigue strength

Figure 2 shows the S-N data of the test materials at 77 K with the maximum cyclic stress normalized to the ultimate tensile strength. The PR and FR exhibit a normalized 10^7 cycles fatigue strength of approximately 0.7, which is superior to the ST of 0.5. The data plots are classified into the surface crack initiation (open) and subsurface crack initiation (solid). The fatigue crack initiation site shifted from the specimen surface to the specimen interior in the longer-life range. For the ST, the sharp drop in fatigue strength over 10^6 cycles was associated with subsurface crack initiation failure. Both the PR and FR materials showed significantly improved high-cycle fatigue strength at 77 K, while the increase in fatigue strength in the low-cycle regime was almost proportional to the increase in their tensile strength.

3.2. Crack initiation sites

Figures 3(a) and 3(b) show the crack initiation sites of the FR at the specimen surface and the specimen interior, respectively. The subsurface crack initiation sites of the FR and ST were consisted of one or more facets and no defects such as inclusions were detected there. For the PR, inclusions were detected at the subsurface crack initiation site as shown in Figure 3(c), where O, Al, Mg, Si and Mn elements were detected by EDS analysis. Therefore, the inclusions are inferred to be composite oxides, i.e., $MgO\text{-}Al_2O_3$ spinel and $MnO\text{-}SiO_2$ rhodonite.

3.3. Subsurface crack initiation site size

At low magnification, the subsurface crack initiation sites appear flat and are inclined to the principal stress axis. In this study, the subsurface crack initiation site is considered to be generated by microcracking and its growth. Then, the subsurface crack initiation sites are defined as the whole of the inclined area that does not place on the fatigue crack propagation plane. Thus, the initiation site gives a Stage I crack and is considered to be equivalent to that of an elliptical initial crack in a plate. The crack length 2a was determined with an orthographic projection on the main crack propagation plane; the direction of the crack length was parallel to the initial crack propagation direction. According to the above, the approximate equation to the stress intensity factor range at the subsurface crack tip can be expressed as follows:

$$\Delta K_{Imax} = A\Delta\sigma_{\max}\sqrt{\pi \cdot 2a} \quad (1)$$

where $\Delta\sigma_{max}$ is the maximum cyclic stress range, 2a is the crack length of the subsurface crack initiation site, and A is the stress intensity coefficient.

Figure 4 shows the dependence of the subsurface crack size on the maximum cyclic stress for the materials, although the number of data plots is small. When the curves of $\Delta\sigma_{max}\sqrt{2a}$= 4.5 MPa$\sqrt{m}$ and 7.1 MPa$\sqrt{m}$ are superimposed in Figure 4, all the data plots are mostly in a range between them. Basically, the subsurface crack size increases regardless of the materials as the maximum cyclic stress decreases. In fact, specimens with a large subsurface crack failed at lower stress levels. Therefore, there may be a threshold condition, ΔK_{Imax} = constant, at any stress level where subsurface crack initiation occurs. It is proposed that the main crack (Stage II) starts to propagate at any stress level when the local stress intensity factor range around the subsurface crack (Stage I) exceeds a constant [3,8].

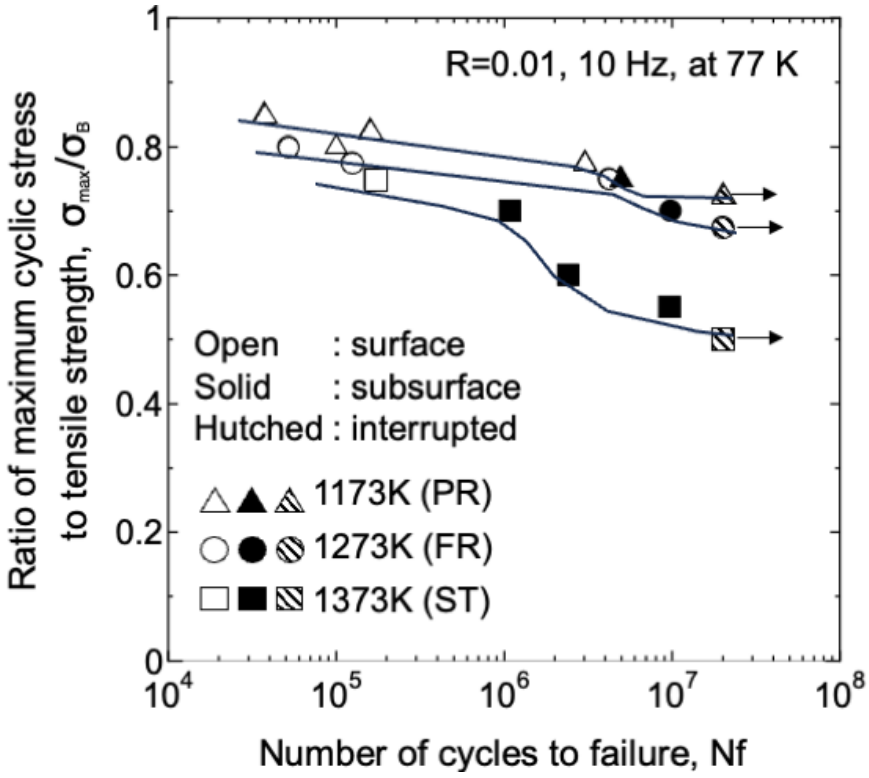

Figure 2. S-N data at 77 K for PR, FR, and ST materials.

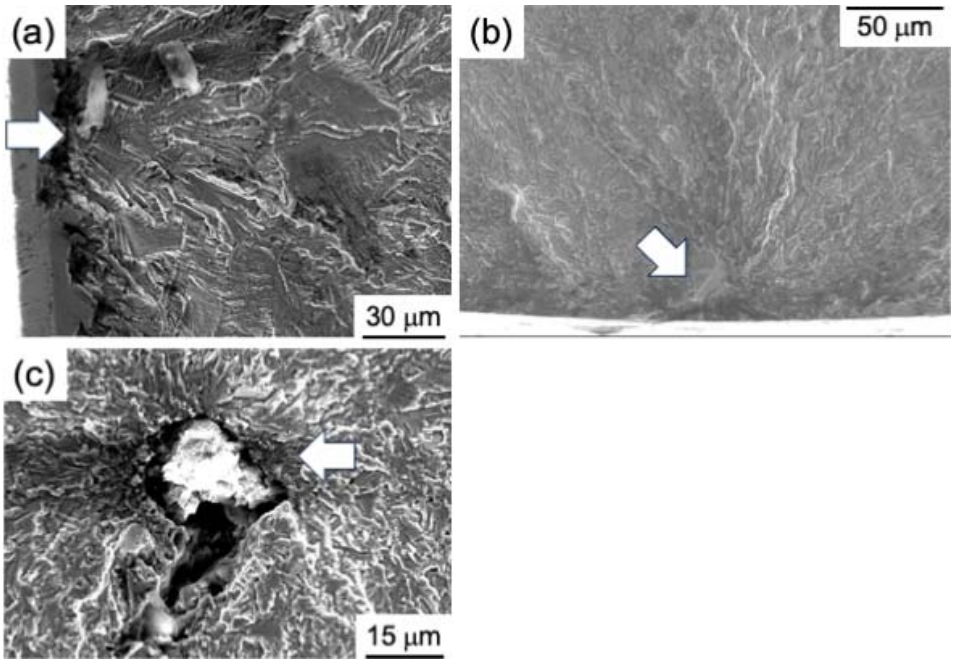

Figure 3. Crack initiation sites at (a) the specimen surface (FR, σ_{max}= 1267 MPa, N_f= 4,220,513 cycles), (b) the specimen interior (FR, σ_{max}= 1183 MPa, N_f = 9,799,376 cycles), and (c) the subsurface inclusion (PR, σ_{max}= 1331 MPa, N_f = 4,891,177 cycles). Arrows show the crack initiation sites.

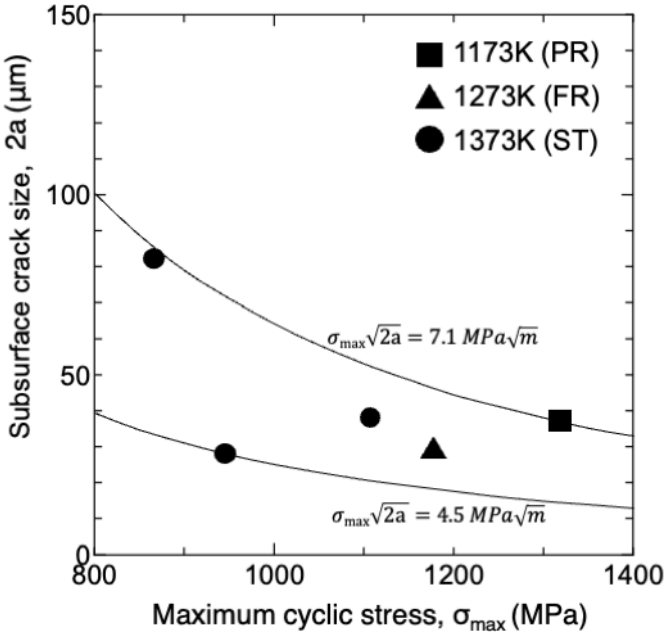

Figure 4. Correlation of subsurface crack size and maximum cyclic stress.

4. Conclusions

The high-cycle fatigue properties of XM-19 austenitic stainless steel were investigated at 77 K for three types of materials such as partially recrystallized (PR), finely recrystallized (FR), and solution-treated (ST). The fatigue crack initiation site shifted from the specimen surface to the specimen interior in the longer-life range. In the ST material, the sharp drop in fatigue strength over 10^6 cycles was related to subsurface crack initiation failure. Both the PR and FR materials showed significantly improved high-cycle fatigue strength at 77 K, while the increase in fatigue strength in the low-cycle regime was almost proportional to the increase in their tensile strength.

5. References

[1] McRae D M, Balachandran S and Walsh R P 2017 *IOP Conf. Ser. Mater. Sci. Eng.* **279** 012001
[2] Kato T, Kato Y, Umezawa O, Ono Y, Yuri T, Nishimura A and Kumagai S. 2022 *IOP Conf. Ser. Mater. Sci. Eng.* **1241**, 012001
[3] Umezawa O and Nagai K 1997 *ISIJ Inter.* **37** 1170–1179
[4] Umezawa O 2021 *Mater. Performance Character.* **10(2)** 3–15
[5] Morita M and Umezawa O 2012 *ISIJ Inter.* **52** 1153–1161
[6] Umezawa O 2004 *Metall. Mater. Trans. A* **35** 543–553
[7] Umezawa O 2009 I*SIJ Inter*. **49** 1624–1629
[8] Umezawa O and Nakai K 1998 *Metall. Mater. Trans. A* **29** 809–822